PHYSICAL REVIEW B VOLUME 26, NUMBER 8 15 OCTOBER 1982

Lattice-dynamical model for graphite

R. Al-Jishi
Department of Physics and Center for Materials Science and Engineering, Massachusetts Institute of Technology, Cambridge, Massachusetts 02139

G. Dresselhaus
Francis Bitter National Magnet Laboratory, Massachusetts Institute of Technology, Cambridge, Massachusetts 02139

(Received 20 November 1981; revised manuscript received 22 February 1982)

The lattice dynamics of pristine graphite is presented with the use of a Born—von Kármán model. With the consideration of interactions to fourth neighbor both intraplane and interplane, good agreement is simultaneously obtained with ir, Raman, and inelastic neutron scattering measurements of lattice modes and with the measured elastic constants. The second-order Raman spectrum is also calculated and compared with experiment.

I. INTRODUCTION

The recent interest in graphite and its intercalation compounds has led us to reexamine the lattice dynamics for pristine graphite. Our investigation was motivated by a desire to explain the recently reported second-order Raman spectra in pristine graphite[1-3] and by the fact that the lattice-dynamical models for the intercalation compounds are based on that for pristine graphite.[4] A number of lattice-dynamical models have been published over the past several years.[5-9] These models require additional terms or interactions in order to fit all the recent experimental data. In particular, the most frequently used model for graphite by Maeda *et al.*[5] does not fit the experimental data for the elastic constants or the low-frequency M-point modes as given in Table I. This table also lists experimental values for the first-order high- and low-frequency Raman-active E_{2g} modes, the infrared-active E_{1u} and A_{2u} modes, and the low frequency Γ- and M-point modes determined from inelastic neutron scattering experiments, in addition to the measured elastic constants.[10,11] It is the objective of this paper to develop a model that simultaneously fits all the experimental values in Table I and to use this model to calculate the second-order Raman spectrum for pristine graphite.

The staging superlattice associated with intercalation compounds suggests that an understanding of the modes in intercalated graphite could lead to improved models for calculating dispersion curves for pristine graphite, particularly for the low- and high-frequency branches away from $k=0$. Such an approach was used by Feldman *et al.*[12] for the layered material SiC on which they carried out Raman experiments and used the polytypes to establish a superlattice and to infer the optical phonon branches.

The Born—von Kármán model presented here makes use of the lowest-order interaction terms required to fit the experimental data. In this connection, it was necessary to extend the Maeda model to include up to fourth-neighbor in-plane and out-of-plane interactions. The density of states calculated from this model has peak shifts as large as ~ 150 cm^{-1} relative to the Maeda model for some of the low-frequency features. A calculation of the second-order Raman spectrum was carried out assuming the electron—LA-phonon coupling is the dominant light-scattering mechanism. The resulting calculation yields good agreement with the observed second-order Raman spectrum, though the force constants of our model were not adjusted to fit the second-order Raman spectrum.

II. MODEL FOR PHONON-DISPERSION RELATIONS

Graphite is a hexagonal crystal with four atoms per primitive cell. The unit cell has four atoms, labeled 1, 2, 3, and 4 in Fig. 1; the second, third, and fourth in-plane neighbors are denoted by 5, 6, and 7, respectively, whereas labels 8 and 9 refer to the third and fourth out-of-plane neighbors, respectively. The primitive lattice vectors are given by

TABLE I. Experimental lattice mode frequencies (cm^{-1}) and elastic constants (10^{11} dyn/cm^2) in graphite and comparison to model calculations by Maeda *et al.* (Ref. 5) and the present work.

	Observed	Maeda[a]	Present calculation
$\omega(E_{2g_2})$	1582[b]	1575	1582
$\omega(E_{1u})$	1587[c]	1574	1587
$\omega(A_{2u})$	868[d]	850	867
$\omega(E_{2g_1})$	42[e]	44	42
$\omega(B_{1g_1})$	127[f]	127	127
$\omega_{\text{TA}}(M \text{ point})$	~465[f]	~290	465
$\omega_{\text{TO}}(M \text{ point})$	~480[f]	~300	478
$C_{11}=C_{22}$	106.0[g]	145.0	106.0
C_{66}	44.0[g]	44.0	45.0
C_{33}	3.65[g]	3.65	3.69
C_{13}	1.50[g]	−0.06	1.50
C_{44}	0.40[g]	0.06	0.42
$C_{55}=C_{44}$	0.40	0.35	0.42

[a] Calculated from the constants of Ref. 5.
[b] References 27–29.
[c] References 29 and 30.
[d] Reference 29.
[e] Reference 16.
[f] Reference 6.
[g] References 10 and 11.

$$\vec{a}_1=(a_0,0,0)\,,\quad \vec{a}_2=(a_0/2,a_0\sqrt{3}/2,0)\,,\quad \vec{a}_3=(0,0,c_0) \tag{1}$$

where $a_0=2.46$ Å and $c_0=6.70$ Å.

The 12×12 dynamical matrix is constructed using the site representation and is written as

$$D(\vec{q})=\begin{vmatrix} D(\vec{q},11) & D(\vec{q},12) & D(\vec{q},13) & D(\vec{q},14) \\ D(\vec{q},21) & D(\vec{q},22) & D(\vec{q},23) & D(\vec{q},24) \\ D(\vec{q},31) & D(\vec{q},32) & D(\vec{q},33) & D(\vec{q},34) \\ D(\vec{q},41) & D(\vec{q},42) & D(\vec{q},43) & D(\vec{q},44) \end{vmatrix}\,, \tag{2}$$

where each block $D_{\alpha\beta}(\vec{q},kk')$ is a 3×3 matrix.[13,14] Two forms for $D_{\alpha\beta}(\vec{q},kk')$ appear in the literature.[14] We make use of both forms (see pp. 327 and 328 of Ref. 14) and denote the corresponding dynamical matrices by $D(\vec{q})$ and $\bar{D}(\vec{q})$. A general formula for the force-constant matrices for any pair of atoms is derived in Ref. 15. In this paper we follow the notation previously used by Maeda *et al.*[5] in which $\phi_r^{(n)}$, $\phi_{ti}^{(n)}$, and $\phi_{to}^{(n)}$ represent, respectively, the radial, in-plane tangential, and out-of-plane tangential force constants between the nth nearest in-plane neighbors. The radial and tangential force constants for interaction between the nth out-of-plane nearest neighbors are denoted by $\hat{\phi}_r^{(n)}$ and $\hat{\phi}_t^{(n)}$, respectively.

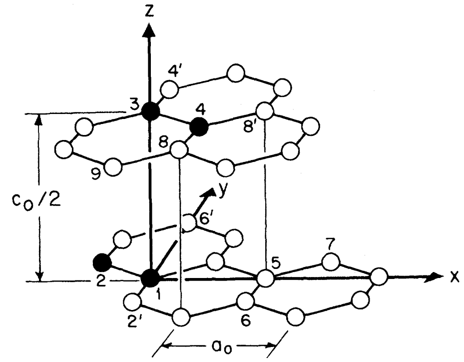

FIG. 1. Lattice sites in graphite showing distinct atoms in the graphite unit cell labeled by dark balls and the numbers 1, 2, 3, and 4. The other in-plane sites are numbered 5, 6, and 7 in order of their distance from site 1, while the third and fourth out-of-plane sites are denoted by 8 and 9.

The calculation for the phonon-dispersion relations utilizes a Born—von Kármán model in which the force constants are determined from the experimental data listed in Table I. Such a model ignores effects arising from the redistribution of the electronic charge when the carbon atoms vibrate. These effects are considered in the shell model, where as a result, faster convergence of the neighbor expansion is obtained in fitting the experimental data. Because of the lack of inelastic neutron scattering data in the range above 500 cm^{-1}, there is not yet enough experimental information available to develop a good shell model for pristine graphite.

At both the Γ and M points in the Brillouin zone we make use of explicit analytic expressions for the mode frequencies in terms of the force constants given in Appendix A. Thus, the force constants are constrained to fit the zone-center frequencies exactly. We further find, in agreement with previous work of Nemanich *et al.*,[16] that in order to fit the experimental observation $\omega(E_{1u})>\omega(E_{2g_2})$, it is necessary to include second-nearest-neighbor out-of-plane interactions, independent of the number of in-plane interactions that are considered. We also find that in order to reproduce the neutron data along the ΓM direction,[6] interactions up to the fourth-nearest in-plane neighbor must be considered. All the elastic constants (see Table I) are expressed in terms of the dynamical matrix elements in Appendix B and thereby can be used in the evaluation of the force constants. We find that if interactions up to the fourth-nearest in-plane neighbor and the second-nearest out-of-plane neighbor are considered, all available data, except C_{13}, can be fitted. Though second-neighbor out-of-plane interactions are sufficient to fit C_{13}, one cannot simultaneously fit the splitting between the E_{1u} and E_{2g} modes without the addition of fourth-nearest out-of-plane neighbor terms. In Appendixes A and B the analytic expressions are given for the eigenvalues at the Γ point in terms of the dynamical matrix elements as well as the frequencies at the M point and the elastic constants. Thus, we solve for the values for the force-constant parameters that give an accurate fit to the zone-center and M-point low-lying frequencies and to the elastic constants.

The model, which includes up to fourth-neighbor in-plane and interplane interactions, has a total of 20 force constants. Not all 20 force constant parameters are uniquely determined by the experimental constraints. Out of the four parameters $\hat{\phi}_r^{(3)}$, $\hat{\phi}_t^{(3)}$, $\hat{\phi}_r^{(4)}$, and $\hat{\phi}_t^{(4)}$, which were introduced to account for the experimental value of C_{13}, only one is really needed, either $\hat{\phi}_r^{(4)}$ or $\hat{\phi}_t^{(4)}$, or a combination of them. Thus with the experimental data set in Table I, there is some ambiguity in choosing some of the values for the force-constant parameters. Taking these ambiguities into account, the convergent set of values given in Table II was selected.

In Fig. 2 we show the calculated dispersion curves based on this model. The most significant difference between these results and those of the Maeda model[5] lies in the low-frequency region along the ΓM axis. This difference is most clearly seen in the phonon density of states $G(\omega)$ vs ω spectrum shown in Fig. 3, which was calculated using the Gilat-Raubenheimer method.[17] The main features of the density-of-states spectrum correspond to peaks at $\omega\simeq 1624$, 1535, 1365, 1345, 1260, 850, 575, 470, and 130 cm^{-1}. The dominant peak at ~ 1350 cm^{-1} is responsible for the disorder-induced Raman line in imperfectly ordered graphite.[18] The peaks at 1624 and 1345 cm^{-1} result from extrema in the phonon-dispersion curve along the ΓK direction. The peaks at 1535, 1365, 850, 575, and 470 cm^{-1} are due to M-point zone-edge phonons, whereas the peak at 1260 cm^{-1} is due to K-point phonons and that at 130 cm^{-1} results from

TABLE II. Values of the force constant parameters in dyn/cm.

Radial	Tangential	
$\phi_r^{(1)}=312\,520.0$	$\phi_{ti}^{(1)}=267\,480.0$	$\phi_{to}^{(1)}=86\,545.0$
$\phi_r^{(2)}=120\,920.0$	$\phi_{ti}^{(2)}=-63\,731.0$	$\phi_{to}^{(2)}=-9312.2$
$\phi_r^{(3)}=27\,978.0$	$\phi_{ti}^{(3)}=19\,000.0$	$\phi_{to}^{(3)}=12\,695.0$
$\phi_r^{(4)}=-25\,508.0$	$\phi_{ti}^{(4)}=9488.0$	$\phi_{to}^{(4)}=-5498.4$
$\hat{\phi}_r^{(1)}=2746.9$	$\hat{\phi}_t^{(1)}=-5934.1$	
$\hat{\phi}_r^{(2)}=595.52$	$\hat{\phi}_t^{(2)}=1271.2$	
$\hat{\phi}_r^{(3)}=-473.88$	$\hat{\phi}_t^{(3)}=473.9$	
$\hat{\phi}_r^{(4)}=200.0$	$\hat{\phi}_t^{(4)}=-927.8$	

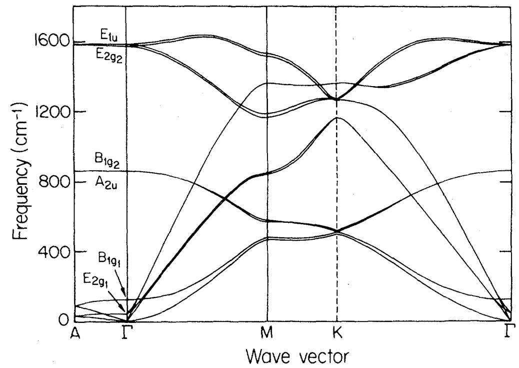

FIG. 2. Phonon dispersion curves in graphite calculated along certain high-symmetry axes.

zone-center phonons. These assignments are in general agreement with those made previously by Nemanich and Solin[1] based on their calculated phonon density of states. It should be noted that no discernible peak results from zone-center phonons at $\sim 1580\ \mathrm{cm}^{-1}$.

III. SECOND-ORDER RAMAN SPECTRUM

A critical test for our phonon-dispersion model is a comparison of the predicted and observed second-order Raman spectrum. Since light scattering by phonons takes place via electrons, the Raman cross section is determined by both the electron-phonon coupling and the phonon density of states. The electron-phonon interaction in turn depends on both wave vector and polarization of the phonon branch. Furthermore, phonons with different wave vectors ($\pm\vec{q}$) and belonging to different branches can also contribute to the second-order Raman cross section.

In second-order Raman scattering, the incident photon is annihilated, a scattered photon is created, and two phonons are emitted or absorbed or one is emitted and the other is absorbed. This is expressed through the electron-photon and electron-phonon interaction. The second-order Raman cross-section is given by[13]

$$\frac{d^2\sigma}{d\Omega\, d\omega} = \sum_{i,q} W(\vec{q},i)\delta(\omega-\omega'-2\omega(\vec{q},i)) \,, \tag{3}$$

where $\vec{q}$, i, and $\omega(\vec{q},i)$ denote the phonon wave vector, branch, and frequency, respectively. The scattering cross section is thus a weighted density of states in which the weight function $W(\vec{q},i)$ is proportional to the square of the second-order Raman tensor. To obtain $W(\vec{q},i)$, we examine the types of processes involved in second-order Raman scattering in graphite. The processes illustrated in Figs. 4(a) and 4(b) are important for the calculations presented here. Other higher-order processes include iterations of the first-order process, giving rise to zone-center contributions to the second-order Raman transitions as well as processes involving interband electron-phonon scattering; processes with two decoupled loops involve a higher order in perturbation theory and can be neglected,[19] whereas processes 4(a) and 4(b) give a continuous spectrum. Processes where the electron (or the hole) scatters a phonon twice are incorporated into processes of type 4(a) through a renormalization of the electron—two-phonon vertex.

In our calculation we assume that the dependence of the second-order Raman transitions on the electron-phonon interaction is the same whether the two phonons are emitted simultaneously [process 4(a)] or sequentially [process 4(b)]. Although this approximation is adopted in order to simplify the calculation, we expect that the magnitude of the interaction is correctly estimated. Consequently, we explicitly consider process 4(b) only. The Raman tensor is proportional to the product of one-phonon—electron interaction matrix elements in the valence and conduction bands $G(c)G(v)$.[20,21] Since

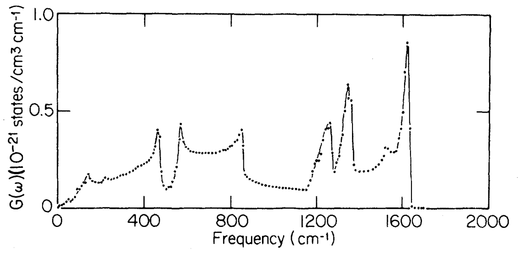

FIG. 3. Phonon density of states for graphite corresponding to the dispersion curves in Fig. 2. The energy resolution is 6 cm^{-1}.

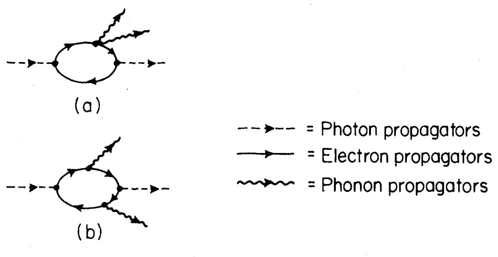

FIG. 4. Diagrams for some of the important processes which contribute to the second-order Raman cross section.

the Raman cross section is proportional to the square of the Raman tensor, the Raman cross section will be proportional to the fourth power of the one-phonon—electron interaction matrix element. It should be noted that in our work we have neglected the dependence of the electron-phonon interaction matrix element on the band index and wave vector of the electronic states.

The assumption that the electron-phonon coupling is constant throughout the Brillouin zone yields a second-order Raman spectrum proportional to the phonon density of states. To fit the experimental features observed in the second-order Raman spectrum we relaxed the assumption of a constant electron-phonon coupling term and took the value of the electron—LA-phonon coupling constant to be 3.5 times larger than the electron—optic-phonon interaction coupling parameter in order to obtain a best fit to the observed Raman spectrum of graphite.

In general, the phonon modes are not purely optic or acoustic, transverse or longitudinal, but rather they have a mixed character. To proceed with the calculation, we determine the 12-component eigenvector $\vec{V}(\vec{q},i)$, $1 \le i \le 12$, at many points in the Brillouin zone (see, e.g., Table III for results at the Γ point) and then project these eigenvectors along the eigenvectors for the longitudinal-acoustic mode. This projection, denoted by $P_l(\vec{q},i)$, is given by

$$P_l(\vec{q},i)=\vec{T}(\vec{q},i)\cdot\vec{q}/|q| \ , \tag{4}$$

where the three-component vector $\vec{T}(\vec{q},i)$ is related to components of the 12-component normal mode vector $\vec{V}(\vec{q},i)$ by (see Table III)

$$T_j(\vec{q},i)=\sum_{n=0,3} V_{j+3n}(\vec{q},i)/2 \ . \tag{5}$$

The probability that the phonon is an optic phonon

TABLE III. The eigenvectors at the Γ point. Here the subscript a on the E_{1ua} and A_{2ua} modes refers to acoustic. The following parameters are defined by

$$\frac{\nu}{\mu}=[m\omega^2(E_{2g_2})-D_{1,1}(0)+D_{1,7}(0)]/[D_{1,4}(0)-D_{1,10}(0)] \ ,$$

$$\frac{\beta}{\alpha}=[m\omega^2(B_{1g_2})-D_{3,3}(0)+D_{3,9}(0)]/[D_{3,6}(0)-D_{3,12}(0)] \ ,$$

$$\frac{\delta}{\gamma}=[m\omega^2(B_{1g_1})-D_{3,3}(0)+D_{3,9}(0)]/[D_{3,6}(0)-D_{3,12}(0)] \ ,$$

$$\frac{\zeta}{\eta}=[m\omega^2(E_{2g_1})-D_{1,1}(0)+D_{1,7}(0)]/[D_{1,4}(0)-D_{1,10}(0)] \ ,$$

and the eigenvectors are normalized by

$$\alpha^2+\beta^2=\tfrac{1}{2},\ \nu^2+\mu^2=\tfrac{1}{2},\ \gamma^2+\delta^2=\tfrac{1}{2},\ \zeta^2+\eta^2=\tfrac{1}{2} \ .$$

	E_{1u}	E_{1u}	E_{2g_2}	E_{2g_2}	B_{1g_2}	A_{2u}	B_{1g_1}	E_{2g_1}	E_{2g_1}	E_{1ua}	E_{1ua}	A_{2ua}
X_1	$\frac{1}{2}$	0	μ	0	0	0	0	η	0	$\frac{1}{2}$	0	0
Y_1	0	$\frac{1}{2}$	0	μ	0	0	0	0	η	0	$\frac{1}{2}$	0
Z_1	0	0	0	0	α	$\frac{1}{2}$	γ	0	0	0	0	$\frac{1}{2}$
X_2	$-\frac{1}{2}$	0	ν	0	0	0	0	ζ	0	$\frac{1}{2}$	0	0
Y_2	0	$-\frac{1}{2}$	0	ν	0	0	0	0	ζ	0	$\frac{1}{2}$	0
Z_2	0	0	0	0	β	$-\frac{1}{2}$	δ	0	0	0	0	$\frac{1}{2}$
X_3	$\frac{1}{2}$	0	$-\mu$	0	0	0	0	$-\eta$	0	$\frac{1}{2}$	0	0
Y_3	0	$\frac{1}{2}$	0	$-\mu$	0	0	0	0	$-\eta$	0	$\frac{1}{2}$	0
Z_3	0	0	0	0	$-\alpha$	$\frac{1}{2}$	$-\gamma$	0	0	0	0	$\frac{1}{2}$
X_4	$-\frac{1}{2}$	0	$-\nu$	0	0	0	0	$-\zeta$	0	$\frac{1}{2}$	0	0
Y_4	0	$-\frac{1}{2}$	0	$-\nu$	0	0	0	0	$-\zeta$	0	$\frac{1}{2}$	0
Z_4	0	0	0	0	$-\beta$	$-\frac{1}{2}$	$-\delta$	0	0	0	0	$\frac{1}{2}$

is given by

$$P_o^2(\vec{q},i)=1-\sum_{j=1,3} T_j^2(\vec{q},i) \tag{6}$$

so that the proposed weight function will take the form

$$W(\vec{q},i)=[P_o^2(\vec{q},i)+3.5P_l^2(\vec{q},i)]^4 \ . \tag{7}$$

With these assumptions, a good fit to the experimentally observed second-order Raman spectrum[1,2] is obtained. A somewhat better fit is achieved if the weight function contains, in addition, a wave-vector—dependent term that reflects the symmetry of the crystal. The form thus obtained for the weight function is

$$W(\vec{q},i)=F(\vec{q})[P_o^2(\vec{q},i)+3.5P_l^2(\vec{q},i)]^4 \ , \tag{8}$$

in which

$$F(\vec{q})=(1+F_{10}+2.65F_{20}-3.5F_{21})^2 \tag{9}$$

and the wave-vector—dependent symmetrized functions are[22]

$$F_{10}=\{\cos(2\pi k_1/3)+\cos[2\pi(k_1+k_2)/3]+\cos(2\pi k_2/3)\}/3 \ , \tag{10a}$$

$$F_{20}=\{\cos(4\pi k_1/3)+\cos[4\pi(k_1+k_2)/3]+\cos(4\pi k_2/3)\}/3 \ , \tag{10b}$$

$$F_{21}=\{\cos[2\pi(2k_1+k_2)/3]+\cos[2\pi(k_1+2k_2)/3]+\cos[2\pi(k_1-k_2)/3]\}/3 \ , \tag{10c}$$

and the coefficients in Eq. (9) are obtained by fitting the observed second-order Raman spectrum. The function $F(q)$, as given in Eq. (9), transforms as a scalar, which implies that only the A_{1g} symmetry scattering is considered. For polarized incident and scattered light both A_{1g} and E_{2g} symmetries should be considered.

In Fig. 5 we plot the second-order Raman cross section calculated from Eq. (3) using the approximation of Eqs. (8) and (9) for the weight function. The experimental spectrum taken by Elman is from Fig. 3 in Ref. 2. The calculation assumes that the two phonons have equal and opposite wave vectors and are on the same branch of the dispersion curves. It is seen in Fig. 5 that all the experimentally observed peaks are reproduced, suggesting that the observed peaks are overtones rather than a combination of two phonons with different frequencies and wave vectors. This conclusion is in agreement with the earlier assignment of modes by Nemanich and Solin,[1] who carried out a detailed comparison between the observed second-order Raman spectrum and their calculated phonon density of states. It should also be noted that this calculation accounts for the shoulder on the dominant second-order feature, yielding peaks at both ~2700 and ~2730 cm^{-1} and associated with contributions from regions near the K and M points, respectively. Likewise the calculation accounts for the doublet structure at 2435 and 2468 cm^{-1}. Moreover, the two peaks at 2435 and 2468 cm^{-1} are not reproduced in the correct position in other lattice-dynamics models[5,6] for graphite. In the dispersion curves shown in Fig. 2, the longitudinal-acoustic branch and the optic branch along the ΓM direction couple strongly at a frequency of ~1230 cm^{-1}, and along the ΓK direction a strong coupling occurs near ~1270 cm^{-1}. In the region of strong coupling, a bending of the dispersion curves occurs, giving rise to a minimum in the upper branch and a maximum in the lower branch. These midzone extrema contribute appreciably to the second-order Raman cross section because the phonon modes in the region of strong coupling have large contributions from the longitudinal-acoustic phonon branch, which couples strongly to the electronic states.

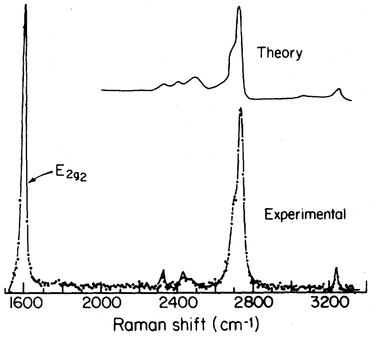

FIG. 5. Calculated and observed second-order Raman spectra for graphite. Calculations follow from the phonon dispersion curves in Fig. 2 (see text). The sharp experimental peak at 2335 cm^{-1} has not been reported by other workers and may not be associated with Raman scattering from graphite.

IV. CONCLUSIONS

The model for the phonon-dispersion relations presented here is consistent with all the currently available experimental data on the zone-center modes, the low-frequency phonon dispersion relations along the ΓM and ΓA directions, the elastic constants, and the dominant features observed in the second-order Raman spectrum. The analytic expressions derived for the frequencies at the M point provide important constraints for the evaluation of the force-constant parameters, as new experimental information becomes available. This model represents an excellent basis for our calculation of the lattice dynamics for intercalated graphite.[23]

ACKNOWLEDGMENTS

We gratefully acknowledge discussions with Professor M. S. Dresselhaus, Dr. S. Y. Leung, and support from AFOSR Contract No. F49620-81-C-0006. The Francis Bitter National Magnet Laboratory is supported by the National Science Foundation.

APPENDIX A: Γ- AND M-POINT MODES OF THE GRAPHITE CRYSTAL

Hexagonal graphite with AB stacking has D_{6h}^4 symmetry. A consequence of this is that at both Γ and M points, the group of the wave vector has the inversion operation I as a symmetry element. Thus a factorization of the dynamical matrix results,[14] which can be expressed as

$$D(\vec{q})=\begin{vmatrix} H & S \\ S^* & H^* \end{vmatrix}, \tag{A1}$$

where H and S are 6×6 Hermitian and symmetric matrices, respectively. Since $D(\vec{q})$ is real at both Γ and M points, it follows that $H^*=H$ and $S^*=S$.

A unitary transformation will transform the matrix $D(\vec{q})$ in the form of Eq. (A1) into

$$\hat{D}(\vec{q})=\begin{vmatrix} H+S & 0 \\ 0 & H-S \end{vmatrix}, \tag{A2}$$

and the diagonalization of the dynamical matrix at the Γ and M points is reduced to diagonalizing two 6×6 matrices.

The zone-center normal modes have the symmetries given by

$$\Gamma_i=2E_{1u}+2E_{2g}+2A_{2u}+2B_{1g}\ . \tag{A3}$$

The Γ-point eigenvalues and eigenvectors for the Raman and infrared-active modes were previously calculated by Maradudin.[24] Using the notation of the present work, the eigenvalues of the dynamical matrix obtained analytically and are given by

$$m\omega^2(E_{1ua})=0\ , \tag{A4a}$$

$$m\omega^2(E_{1u})=2[D_{1,1}(0)+D_{1,7}(0)]\ , \tag{A4b}$$

$$m\omega^2(E_{2g})=[C_1(0)\pm H_1(0)]/2\ , \tag{A4c}$$

$$m\omega^2(B_{1g})=[C_3(0)\pm H_3(0)]/2\ , \tag{A4d}$$

$$m\omega^2(A_{2ua})=0\ , \tag{A4e}$$

$$m\omega^2(A_{2u})=2[D_{3,3}(0)+D_{3,9}(0)]\ , \tag{A4f}$$

where $C_i(0)$ and $H_i(0)$ are obtained at $\vec{q}=0$ from $D_{i,j}(\vec{q})$ by

$$C_i(\vec{q})=D_{i,i}(\vec{q})-D_{i,i+6}(\vec{q})+D_{i+3,i+3}(\vec{q})-D_{i+3,i+9}(\vec{q})\ , \tag{A5}$$

$$H_i^2(\vec{q})=[D_{i,i}(\vec{q})-D_{i,i+6}(\vec{q})-D_{i+3,i+3}(\vec{q})+D_{i+3,i+9}(\vec{q})]^2+4[D_{i,i+3}(\vec{q})-D_{i,i+9}(\vec{q})]^2 \tag{A6}$$

for $i=1,2,3$. The eigenvectors at the zone center are given in Table III.

At the M point, the normal modes have symmetries

$$M_i=2M_{1+}+2M_{2+}+2M_{3+}+2M_{2-}+2M_{3-}+2M_{4-}\ , \tag{A7}$$

where the notation of Ref. 25 is followed in making the symmetry assignments. The eigenvalues of the dynamical matrix at the M point are given by

$$m\omega^2(M_{1+})=[C_2(\vec{q}_M)\pm H_2(\vec{q}_M)]/2\ , \tag{A8a}$$

$$m\omega^2(M_{2+})=[C_1(\vec{q}_M)\pm H_1(\vec{q}_M)]/2\ , \tag{A8b}$$

$$m\omega^2(M_{3+})=[C_3(\vec{q}_M)\pm H_3(\vec{q}_M)]/2\ , \tag{A8c}$$

$$m\omega^2(M_{2-})=[A_3(\vec{q}_M)\pm B_3(\vec{q}_M)]/2\ , \tag{A8d}$$

$$m\omega^2(M_{3-})=[A_1(\vec{q}_M)\pm B_1(\vec{q}_M)]/2\ , \tag{A8e}$$

$$m\omega^2(M_{4-})=[A_2(\vec{q}_M)\pm B_2(\vec{q}_M)]/2\ , \tag{A8f}$$

in which $A_i(\vec{q}_M)$ and $B_i(\vec{q}_M)$ are found from

$$A_i(\vec{q})=D_{i,i}(\vec{q})+D_{i,i+6}(\vec{q})+D_{i+3,i+3}(\vec{q})+D_{i+3,i+9}(\vec{q}) \tag{A9}$$

$$B_i^2(\vec{q})=[D_{i,i}(\vec{q})+D_{i,i+6}(\vec{q})-D_{i+3,i+3}(\vec{q})-D_{i+3,i+9}(\vec{q})]^2+4[D_{i,i+3}(\vec{q})+D_{i,i+9}(\vec{q})]^2 \tag{A10}$$

for $\vec{q}=\vec{q}_M$, and $C_i(\vec{q}_M)$ and $H_i(\vec{q}_M)$ are obtained from Eqs. (A5) and (A6) at $\vec{q}=\vec{q}_M$.

APPENDIX B: ELASTIC CONSTANTS

The elastic constants to be fitted are C_{11}, C_{33}, C_{44}, C_{66}, and C_{13} along with the relation $C_{44}=C_{55}$, which is equivalent to requiring that the square-bracket matrix elements in Refs. 13 and 14 satisfy the identity $[33,11]=[11,33]$, the only one among the Huang relations that is not automatically satisfied in the case of the graphite crystal.[26]

The relations expressing the elastic constants in terms of the dynamical matrix elements are given by

$$C_{33}=[33,33]=\frac{1}{2}\left.\frac{\partial^2 Q_{33}}{\partial q_z^2}\right|_{q_z=0}, \tag{B1}$$

$$C_{55}=[11,33]=\frac{1}{2}\left.\frac{\partial^2 Q_{55}}{\partial q_z^2}\right|_{q_z=0}, \tag{B2}$$

$$C_{44}=[33,11]=\frac{1}{2}\left.\frac{\partial^2 Q_{44}}{\partial q_y^2}\right|_{q_y=0}, \tag{B3}$$

$$\begin{aligned} C_{13}&=2[13,13]-[33,11]\\ &=2\left.\frac{\partial^2 Q_{13}}{\partial q_y \partial q_z}\right|_{q_y=q_z=0}-C_{44}\,, \end{aligned} \tag{B4}$$

where:

$$\begin{aligned} Q_{33}=2[&2\bar{D}_{3,3}(\vec{\mathrm{q}})+2\bar{D}_{3,6}(\vec{\mathrm{q}})+\bar{D}_{3,9}(\vec{\mathrm{q}})\\ &+2\bar{D}_{3,12}(\vec{\mathrm{q}})+\bar{D}_{6,12}(\vec{\mathrm{q}})]/v\,, \end{aligned} \tag{B5}$$

$$\begin{aligned} Q_{55}=2[&2\bar{D}_{2,2}(\vec{\mathrm{q}})+2\bar{D}_{2,5}(\vec{\mathrm{q}})+\bar{D}_{2,8}(\vec{\mathrm{q}})\\ &+2\bar{D}_{2,11}(\vec{\mathrm{q}})+\bar{D}_{5,11}(\vec{\mathrm{q}})]/v\,, \end{aligned} \tag{B6}$$

$$Q_{44}=Q_{33}\,, \tag{B7}$$

$$Q_{13}=2[\mathrm{Re}\bar{D}_{2,12}(\vec{\mathrm{q}})+\mathrm{Re}\bar{D}_{5,12}(\vec{\mathrm{q}})]/v\,, \tag{B8}$$

and v is the volume of a unit cell given by $\sqrt{3}a_0^2c_0/2$.

In writing C_{11} and C_{66}, perturbation theory is used, and the eigenvectors at the Γ point are needed. We make the approximation that the nonzero quantities given in Table III are replaced by $-\frac{1}{2}$ or $+\frac{1}{2}$ depending on the sign of the quantity under consideration. This approximation gives rise to a negligible error in evaluating C_{11} and C_{66}, which, as a matter of fact, is much smaller than the error in the experimental measurements. Thus C_{11} and C_{66} are then given by

$$\begin{aligned} C_{66}=\frac{1}{v}\Bigg[&\frac{\partial^2}{\partial q_y^2}[2D_{1,1}(\vec{\mathrm{q}})+2D_{1,4}(\vec{\mathrm{q}})+D_{1,7}(\vec{\mathrm{q}})+2D_{1,10}(\vec{\mathrm{q}})+D_{4,10}(\vec{\mathrm{q}})]_{q_y=0}\\ &-\left\{\frac{\partial}{\partial q_y}[2\,\mathrm{Im}D_{4,1}(\vec{\mathrm{q}})+\mathrm{Im}D_{4,10}(\vec{\mathrm{q}})+\mathrm{Im}D_{7,1}(\vec{\mathrm{q}})]_{q_y=0}\right\}^2\Big/m\omega^2(E_{2g_2})\\ &-\left\{\frac{\partial}{\partial q_y}[2\,\mathrm{Im}D_{1,10}(\vec{\mathrm{q}})+\mathrm{Im}D_{4,10}(\vec{\mathrm{q}})+\mathrm{Im}D_{7,1}(\vec{\mathrm{q}})]_{q_y=0}\right\}^2\Big/m\omega^2(E_{2g_1})\Bigg]\,. \end{aligned} \tag{B9}$$

C_{11} is given by the same expression as C_{66} except that every matrix element $D_{m,n}(\vec{\mathrm{q}})$ in the above expression is replaced by $D_{m+1,n+1}(\vec{\mathrm{q}})$.

---

[1] R. J. Nemanich and S. A. Solin, Phys. Rev. B 20, 392 (1979).

[2] R. Al-Jishi, B. S. Elman, and G. Dresselhaus, Extended Abstracts of the 15th Biennial Conference on Carbon, Univ. of Penn., p. 34 (1981).

[3] M. S. Dresselhaus and G. Dresselhaus, in *Light Scattering in Solids*, Vol. 51 of *Topics in Applied Physics*, edited by M. Cardona and G. Güntherodt (Springer, Berlin, 1982), p. 2.

[4] S. Y. Leung, G. Dresselhaus, and M. S. Dresselhaus, Solid State Commun. 38, 175 (1981).

[5] M. Maeda, Y. Kuramoto, and C. Horie, J. Phys. Soc. Jpn. 47, 337 (1979).

[6] R. Nicklow, N. Wakabayashi, and H. G. Smith, Phys. Rev. B 5, 4951 (1972).

[7] J. A. Young and J. U. Koppel, J. Chem. Phys. 42, 357 (1965).

[8] A. A. Ahmadieh and H. A. Rafizadeh, Phys. Rev. B 7, 4527 (1973).

[9] K. K. Mani and R. Ramani, Phys. Status Solidi 61, 659 (1974).

[10] O. L. Blakslee, D. G. Proctor, E. J. Seldin, G. B. Spence, and T. Weng, J. Appl. Phys. 41, 3373 (1970).

[11] E. J. Seldin and C. W. Nezbeda, J. Appl. Phys. 41, 3389 (1970).

[12] D. W. Feldman, J. H. Parker, Jr., W. J. Choyke, and L. Patrick, Phys. Rev. 173, 787 (1968).

[13] G. Venkataraman, L. A. Feldkamp, and V. C. Sinha,

Dynamics of Perfect Crystals (MIT Press, Cambridge, Mass., 1975).

[14] Melvin Lax, *Symmetry Principles in Solid State and Molecular Physics* (Wiley, New York, 1974).

[15] S. Y. Leung, G. Dresselhaus, and M. S. Dresselhaus, Phys. Rev. B 24, 6083 (1981).

[16] R. J. Nemanich, G. Lucovsky, and S. A. Solin, in *Proceedings of the International Conference on Lattice Dynamics,* edited by M. Balkanski (Flammarion, Paris, 1975), p. 619.

[17] G. Gilat and L. J. Raubenheimer, Phys. Rev. 144, 390 (1966).

[18] P. Lespade, R. Al-Jishi, and M. S. Dresselhaus, Carbon (in press).

[19] B. A. Weinstein and M. Cardona, Phys. Rev. B 8, 2795 (1973).

[20] A. K. Ganguly and J. L. Birman, Phys. Rev. 162, 806 (1967).

[21] R. Loudon, Proc. R. Soc. London Ser. A 275, 218 (1963).

[22] L. G. Johnson and G. Dresselhaus, Phys. Rev. B 7, 2275 (1973).

[23] R. Al-Jishi and G. Dresselhaus, following paper, Phys. Rev. B 26, 4523 (1982).

[24] A. A. Maradudin, Phys. Rev. B 13, 658 (1976).

[25] S. C. Miller and W. F. Love, *Table of Irreducible Representations of Space Groups and Corepresentations of Magnetic Space Groups* (Pruett, Boulder, Colo., 1967).

[26] A. P. P. Nicholson and D. J. Bacon, J. Phys. C 10, 2295 (1977).

[27] F. Tuinstra and J. L. Koenig, J. Chem. Phys. 53, 1126 (1970).

[28] L. J. Brillson, E. Burstein, A. A. Maradudin, and T. Stark, in *The Physics of Semimetals and Narrow Gap Semiconductors,* edited by D. L. Carter and R. T. Bate (Pergamon, Oxford, 1971), p. 187.

[29] R. J. Nemanich, G. Lucovsky, and S. A. Solin, Mater. Sci. Eng. 31, 157 (1977).

[30] R. A. Friedel and G. C. Carlson, J. Phys. C 75, 1149 (1971).